Evaluation of deformable registration of patient lung 4DCT with subanatomical region segmentations

Ziji Wu[a)]
Department of Radiation Oncology, Massachusetts General Hospital, 55 Fruit Street, Boston, Massachusetts 02114

Eike Rietzel
Siemens Medical Solutions, Particle Therapy, Henkestrasse 127, 91052 Erlangen, Germany

Vlad Boldea
LIRIS Laboratory, Université Lumière Lyon, Lyon, France

David Sarrut
Léon Bérard Anti-Cancer Center, 28 rue Laënnec, 69373 Lyon, France and CREATIS Laboratory, UMR CNRS 5220, Inserm U 630 Lyon, France

Gregory C. Sharp
Department of Radiation Oncology, Massachusetts General Hospital, 55 Fruit Street, Boston, Massachusetts 02114

(Received 10 May 2007; revised 28 November 2007; accepted for publication 30 November 2007; published 30 January 2008)

Deformable registration is needed for a variety of tasks in establishing the voxel correspondence between respiratory phases. Most registration algorithms assume or imply that the deformation field is smooth and continuous everywhere. However, the lungs are contained within closed invaginated sacs called pleurae and are allowed to slide almost independently along the chest wall. This sliding motion is characterized by a discontinuous vector field, which cannot be generated using standard deformable registration methods. The authors have developed a registration method that can create discontinuous vector fields at the boundaries of anatomical subregions. Registration is performed independently on each subregion, with a boundary-matching penalty used to prevent gaps. This method was implemented and tested using both the B-spline and Demons registration algorithms in the Insight Segmentation and Registration Toolkit. The authors have validated this method on four patient 4DCT data sets for registration of the end-inhalation and end-exhalation volumes. Multiple experts identified homologous points in the lungs and along the ribs in the two respiratory phases. Statistical analyses of the mismatch of the homologous points before and after registration demonstrated improved overall accuracy for both algorithms. [DOI: 10.1118/1.2828378]

Key words: deformable image registration, validation, 4DCT

I. INTRODUCTION

Deformable registration is used for a variety of tasks in four-dimensional (4D) radiotherapy, including contour propagation, treatment adaptation, dosimetric evaluation, and 4D optimization.[1–11] Several different core algorithms have been proposed and validated for nonrigid registration of CT images for cancer patients. For example, Wang *et al.* used an accelerated Demons algorithm and evaluated it on prostate, head-and-neck, and lung cases.[12] They accelerated the Demons algorithm by introducing an active force along with an adaptive force strength adjustment during the iterative process. The improvements led to not only a speedup over the original algorithm but also a high tolerance of large organ deformations. Yang *et al.* employed an in-house B-spline (BSP) image registration software with normalized cross-correlation metric to evaluate cone beam CT for dose calculation.[13] A variety of other methods include, but are not limited to, optical flow, thin-plate spline, calculus of variations, and finite element methods with different motion models.[2,14–19]

In nearly every implementation of deformable registration, regularization and smoothness penalties are imposed to achieve a smooth and continuous deformation vector field. While regularization is required because deformable registration is an ill-posed problem, it is difficult for these algorithms to create true discontinuities. In particular, these algorithms tend to have reduced accuracy near the pleural boundary, where the lungs can slide against the chest wall to create discontinuities of more than two centimeters. To solve this problem, we have developed an approach for registration of 4DCT that respects the discontinuity at the pleural interface. As described in Rietzel and Chen,[20] the thorax is segmented into moving (lungs, mediastinum, and abdomen) and less-moving (the rest) subregions, and each region is registered separately. In this article, we introduce a boundary-matching criterion that helps to eliminate gaps between sepa-

rately registered subregions. In addition, we validate the benefits of this method for deformable registration of 4DCT, using both B-spline and Demons algorithms. Homologous points are identified by multiple experts in lungs and on the ribs and statistical analysis is performed. Registration of anatomical subregions with boundary-matching constraints was found to achieve better alignment both in lungs and on the ribs.

II. MATERIAL AND METHODS

We implemented B-spline[21] and Demons[22] deformable registration algorithms in C++ based on the Insight Segmentation and Registration Toolkit. Both algorithms were used to register CT volumes at end-inhalation (EIH) to the one at end-exhalation (EEH). For each algorithm, two types of registration were conducted: (1) registering the entire volume with uniform regularization and (2) registering the moving and less-moving subregions separately while imposing a boundary-matching criterion.

B-spline registration is a parametric method that uses uniform B-spline interpolation to generate a vector field over the volume of interest. B-spline coefficient values are defined at regular intervals along coarse, regular grid, and the deformation field is a smooth interpolation of the coefficient values. The coefficient values are achieved by minimizing a cost metric based on the image intensity differences. A large number of coefficient values makes it possible to represent a wide variety of deformations, but also contributes to long running times for the registration.

In the Demons algorithm, each image is viewed as a set of isointensity contours. The main idea is that a regular grid of forces deforms an image by pushing the contours in the normal direction. The orientation and magnitude of the displacement is derived from the instantaneous optical flow equation. The Demons algorithm relies on the assumption that pixels representing the same homologous point on an object have the same intensity on both the fixed and moving images to be registered. Hence, this method is particularly suitable for intramodality deformable registration problems.

II.A. Registration with segmentation

In addition to performing deformable registration with uniform regularization as reported earlier by others,[23,24] we have developed an approach for registration of 4DCT that respects the discontinuity at the pleural interface. The thorax in each 4DCT phase for each patient is first segmented semiautomatically by a trained expert into moving and less-moving subregions. The moving subregion consists of lungs, mediastinum, and abdomen, while the less-moving subregion is the rest. Although the pleurae are generally not visible in the 4DCT data, we believe our segmentation is along the pleural interface based on the anatomical knowledge.

Masks are created for each subregion and the subregions are registered separately. To register a single subregion, the image is cropped to include the slightly more than the region of interest. Then, the mask is used to modify the image intensities within the cropped volume. Voxel intensities that belong to the subregion remain unchanged, while voxels that lie outside the subregion are assigned a unique intensity value at the low end of the normal range of values (we use -1200 HU for CT). Then registration proceeds using all of the voxels in the cropped volume, including the voxels with modified intensities. After both registrations are complete, the composite deformation vector field is obtained by using the mask to select displacement values from the appropriate registration result.

The purpose of the intensity assignment procedure is to eliminate gaps between separately registered subregions. The unique intensity values help match the boundaries of the subregions, by imposing a penalty for matching voxels from one subregion with the other. For B-spline registration, the difference in image intensities increases the cost of a misaligned subregion boundary. For Demons registration, the intensity discontinuity at the boundary creates a strong spatial gradient, which pushes voxels toward their correct subregion. In this way, the boundaries of each subregion are forced to match. Yet, the matching does not constrain the sliding motion along the boundary.

The same algorithm parameters were used for both whole-volume registration and subregion registrations. For all the B-spline registrations, we used the third order spline with 50 mm cube control grid size. The cost metric was mean squared voxel intensity difference. A modified limited memory Broyden, Fletcher, Goldfarb, and Shannon minimization algorithm was used for optimization [25]. The standard deviation for the Gaussian smoothing in Demons was 0.5 mm. The maximum number of iterations is set to 50. Both methods used trilinear interpolation. The image resolution for calculation was $1.9\ \text{mm} \times 1.9\ \text{mm} \times 2.5\ \text{mm}$ with small variations between different patient sets.

II.B. Validation method

We evaluated the effect of subregion segmentation on registration results with manually identified points both in the lungs and on the ribs of 4DCT scans for four patients with nonsmall cell lung cancer. 4DCT was acquired on a GE Lightspeed Qx/I four-slice CT scanner. For all patients, the images were scanned at a resolution of $0.9\ \text{mm} \times 0.9\ \text{mm} \times 2.5\ \text{mm}$ and downsampled in the (x, y) plane to $1.9\ \text{mm} \times 1.9\ \text{mm} \times 2.5\ \text{mm}$. Three experts identified points on vessel and airway bifurcations in both lungs, as well as points on and near the tumors. Expert No. 1 identified reference points in the EIH phase and all three experts clicked on the matching points in the EEH phase. Reference points were chosen to be evenly distributed between the apex and base in both lungs. We analyzed the identification accuracy in terms of inter-rater variability, which seems to be acceptable considering the image resolution used. Similarly, two experts clicked on points along ribs on both sides along the superior ridge from the vertebral column to the costal cartilages. To maintain consistency, each expert defined his own reference curve along each rib and reproduced the same curve in the other scan. We examined the magnitude of motions in the left

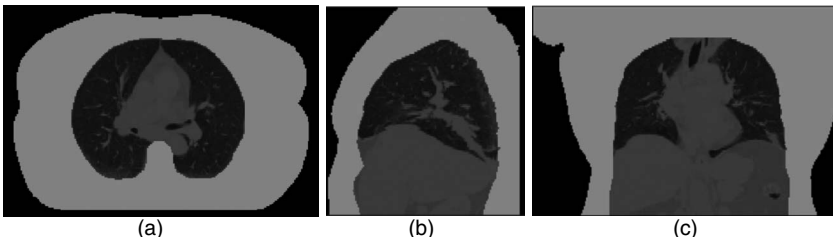

FIG. 1. An example of moving and less-moving subregions. The moving subregion is represented by the gray scale intensities while the less-moving subregion is shown as a homogenous mask. (a) axial view, (b) sagittal view, and (c) coronal view.

and right lungs and on the ribs. Quantitative comparisons were also done to evaluate the benefit of registration with segmentation.

III. RESULTS

III.A. Segmentation illustration

An example of segmentation is displayed in Fig. 1 in axial, sagittal, and coronal views. The moving subregion is represented by the gray scale intensities while the less-moving subregion is shown as a homogenous mask.

III.B. Identification accuracy of the homologous points

As mentioned earlier, we evaluated the effect of subregion segmentation on registration results with manually identified homologous points both in the lungs and on the ribs of 4DCT scans for four patients with nonsmall cell lung cancer. Figure 2 shows two examples of the identified points on vessel and airway bifurcations in the lungs and on the tumors color coded with respect to different raters. There are 17–56 points in lungs for each patient. In addition, between 3 and 7 ribs were identified on each side of each patient, with between 22 and 63 points identified on each rib.

III.C. Magnitude of motions in lungs and on the ribs

Figure 3 displays the magnitude of motion as identified by experts between EIH and EEH respiratory phases in lungs and ribs for patient No. 2, arranged according to their craniocaudal coordinates. The mean magnitude of motion is also plotted as a solid line in the figures. Moving from apex to base, the motion of points in the lungs increases, as shown in Fig. 3(a). The magnitude of motion for the lung points of this patient was 6.74 ± 4.49 mm, with a maximum motion of over 20 mm. The ribs of this patient, however, moved only 1.38 ± 0.67 mm for left ribs and 1.86 ± 0.74 mm for right ribs. While the right and left ribs seem to have somewhat different amount of motion, as illustrated in Fig. 3(b), there is no apparent trend in the craniocaudal direction. This demonstrates the difference between motion in the lungs and chest wall, caused by the sliding of the lungs against the pleural surface.

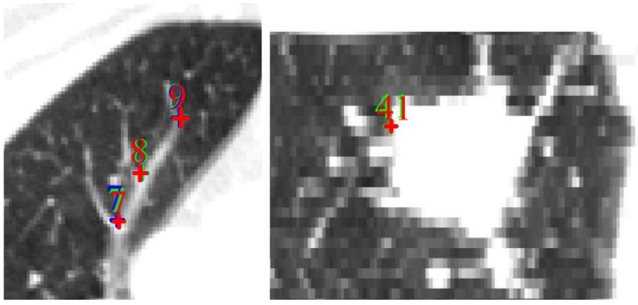

FIG. 2. Point clicking by experts in lungs on vessel and airway bifurcations (left) and tumor (right).

III.D. Visual comparison

Figures 4(a) and 4(d) show the intensity difference map between the warped and fixed images in patient No. 2 for

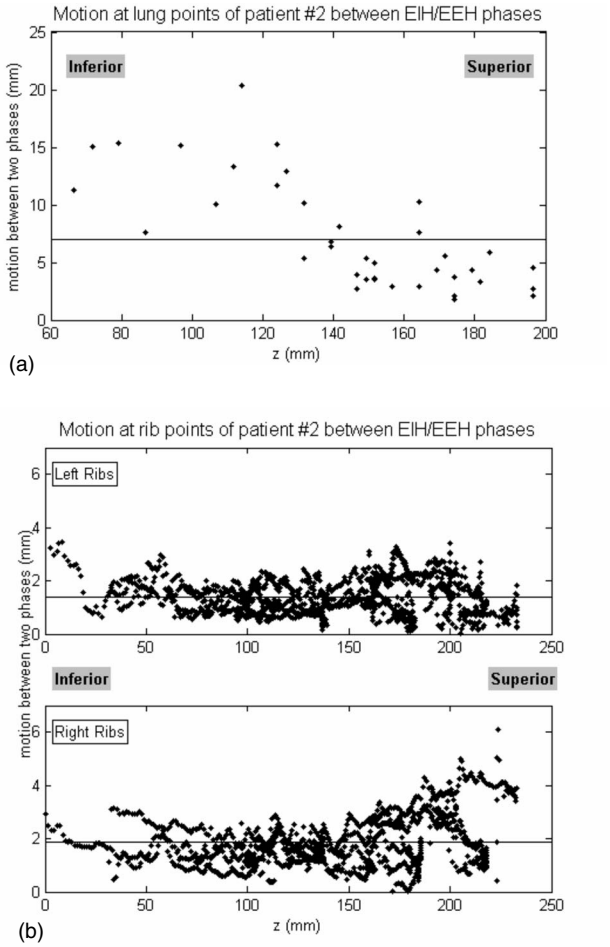

FIG. 3. Magnitude of motions between EIH/EEH phases measured at points in lungs and on ribs as a function of their craniocaudal coordinates for patient No. 2. (a) magnitude of motion in lungs, with the mean shown as a solid line and (b) magnitude of motion on ribs, with the mean shown as a solid line.

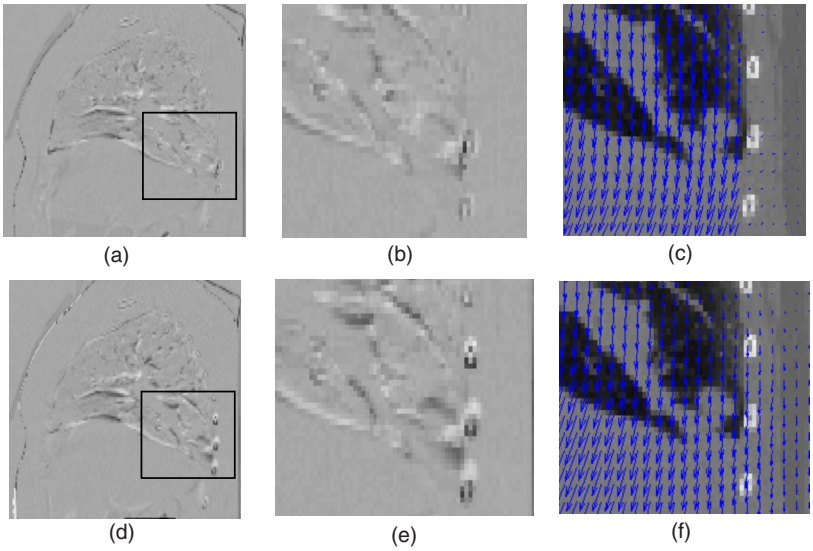

FIG. 4. Registration result comparison on a sagittal plane in patient No. 2. (a) intensity difference map between the warped and fixed images for the BSP registration with segmentation, (b) enlarged view of the posterior pleural interface (highlighted in a), (c) vector field of the posterior pleural interface (highlighted in a), (d) intensity difference map between the warped and fixed images for the BSP registration without segmentation, (e) enlarged view of the posterior pleural interface (highlighted in d), and (f) vector field of the posterior pleural interface (highlighted in d).

B-spline registration done with and without subregion segmentation, respectively. We present here results in sagittal planes for the sake of clarity although the registrations were done on volumetric data. The maps are scaled based on the maximum CT number in the fixed image (MaxVal) so that gray represents identical whereas black and white the signed differences up to the magnitude of the MaxVal. The two maps look similar overall. However, a significant disparity occurs within the posterior chest wall. In the enlarged views of this region, shown in Figs. 4(b) and 4(e), it is evident that the registration with segmentation produced more credible alignment of the ribs than the one without segmentation. Figures 4(c) and 4(f) illustrate the corresponding deformation vector fields in the same area. Along the plural interface, there is a clear discontinuity of the vector field produced by the registration with segmentation, which is consistent with anatomical knowledge. This feature, however, is absent in Fig. 4(f).

III.E. Quantitative analyses

A summary of the distances between homologous points in EIH and EEH respiratory phases for all four patients in lungs and on ribs before and after deformable registration are listed in Table I. The average of the mean distances over all patients is listed in Table II. All registration methods improved the average alignment of the homologous points. For the methods without segmentation, the average alignment errors improved from 3.94 to 3.52 mm for BSP and to 2.93 mm for Demons. For the ones with segmentation, the average alignment errors reduced further to 2.13 mm for BSP and to 2.07 mm for Demons. The improvements are more apparent for points within the lungs where the average distance dropped from 7.85 to 3.50 mm for BSP and 2.93 mm for Demons without segmentation and 2.78 mm for BSP and 2.73 mm for Demons with segmentation.

IV. DISCUSSIONS

IV.A. Inter-rater agreement

The agreement between the corresponding points in lungs identified by different experts on all the patients had a mean distance of 1.34 ± 1.49 mm. Since the experts identified the points on the image volumes with original resolution of about 0.9 mm $\times$ 0.9 mm $\times$ 2.5 mm, we felt this degree of inter-rater variability was acceptable.

IV.B. Improved registration with segmentation

Without segmentation, the improvement in registration of the lungs often comes with a sacrifice in the alignment accuracy of the ribs. The average residual misalignment for rib points was reduced from 3.53 to 1.98 mm for BSP and from 2.92 to 1.74 mm for Demons with the introduction of segmentation. This is foreseeable because the registration methods without segmentation must minimize the cost function over the entire volume and the regularization or smoothing mechanism has to make local compromises around the deformation discontinuities.

With segmentation, registration consistently achieved good alignment in both the lungs and the ribs, as shown in Tables I and II. Compared to registration without segmentation, alignment improved at $p=0.002$ for BSP and $p=0.166$ for Demons. The improvement is lower for Demons because the Demons algorithm has more degrees of freedom, which usually results in a less smooth deformation vector field. This property may or may not be physically desirable depending on the application.

We would like to stress that it is not our intention to compare the B-spline and Demons algorithms, but rather that segmentation of anatomical subregions when there is known discontinuity of the deformation vector field, such as the plural interface, can improve the registration accuracy for both B-spline and Demons algorithms. In addition, although we only compared the registration results with and without seg-

TABLE I. Distance between corresponding points in EIH and EEH phases for four patients.

Patients	(mm)	No reg[a]	BSP no seg[b]	BSP seg[c]	Dem no seg[d]	Dem seg[e]
1	Lungs	6.37 ± 3.49	2.85 ± 1.89	2.12 ± 0.96	2.29 ± 2.94	2.55 ± 3.24
	Left ribs	1.07 ± 0.51	2.93 ± 3.44	1.06 ± 0.64	1.62 ± 1.02	1.31 ± 0.62
	Right ribs	1.66 ± 0.82	2.33 ± 1.01	1.50 ± 0.85	1.93 ± 1.13	1.69 ± 0.82
2	Lungs	6.74 ± 4.49	2.67 ± 1.30	2.73 ± 1.36	2.16 ± 1.83	1.81 ± 1.00
	Left ribs	1.38 ± 0.67	1.96 ± 1.23	1.29 ± 0.76	1.62 ± 0.94	1.42 ± 0.84
	Right ribs	1.86 ± 0.74	3.70 ± 2.85	1.79 ± 1.21	2.23 ± 1.42	2.07 ± 1.38
3	Lungs	11.48 ± 5.90	4.26 ± 2.39	2.80 ± 1.47	3.23 ± 2.72	2.38 ± 1.10
	Left ribs	3.53 ± 1.83	3.37 ± 2.41	2.17 ± 1.18	4.51 ± 3.03	1.81 ± 0.94
	Right ribs	3.91 ± 1.93	8.58 ± 6.72	3.35 ± 2.93	7.84 ± 5.52	2.37 ± 1.52
4	Lungs	6.80 ± 4.85	4.21 ± 2.42	3.48 ± 2.28	4.06 ± 4.21	4.19 ± 4.46
	Left ribs	1.10 ± 0.73	2.49 ± 2.02	1.44 ± 0.70	1.65 ± 0.98	1.48 ± 0.79
	Right ribs	1.32 ± 0.73	3.55 ± 2.25	1.84 ± 1.22	1.99 ± 1.14	1.80 ± 0.94

[a]Distance between corresponding points without registration.
[b]Distance between corresponding points after B-spline registration without segmentation.
[c]Distance between corresponding points after B-spline registration with segmentation.
[d]Distance between corresponding points after Demons registration without segmentation.
[e]Distance between corresponding points after Demons registration with segmentation.

mentation for B-spline and Demon's algorithms for lung 4DCT in this article, we believe the concept can be easily extended to other image registration methods for the applications that deal with deformation field discontinuities.

Previous works have been done to validate methods of registering lung CT volumes. Rietzel and Chen reported 2.1 ± 1.5 mm on five 4DCT data sets with five fiducials each in the lungs using B-spline registration.[20] Coselmon *et al.* attained 1.7, 3.1, and 3.6 mm about the RL, AP, and IS directions by using thin-plate splines to register breath-hold CT images.[15] Li *et al.* reached 0.4 mm registration accuracy on manually located and paired feature points in different patient CT volumes with resolution of 0.5 mm by 0.5 mm and 0.65 mm in their effort to build a human lung atlas.[26] Matsopoulos *et al.* were able to get 6 mm alignment error on average with 15 CT paired data sets by using radial basis functions to register manually identified feature points in lung.[27] Sarrut *et al.* recently proposed a comparison framework for motion estimation methods by using more than 500 landmarks within 4DCT images of lung for three patients.[28]

In addition, there has been considerable research in using structures or regions as part of the registration process. Little *et al.* incorporated independent rigid objects in a modified thin-plate spline based nonrigid registration.[29] Arsigny *et al.*[30] and Commowick *et al.*[31] proposed "fuzzy" regions, which makes the transitions or interpolations between the regions straightforward to handle. These approaches generally do not apply to the case of lung pleurae, where the moving and less-moving regions are abutting and yet sliding against each other with no or little transition region in between. However, in the abdomen when organs such as kidneys and pancreas can be identified in the CT scans and being used as regions of interest, these algorithms may help to improve the registration in the vicinity. Future work needs to be done to extend our method to incorporate these algorithms in the abdominal regions.

IV.C. Segmentation and boundary matching

It is understandable that the quality of the segmentation plays a significant role in the accuracy of the algorithms. Because the image intensity-based cost functions and boundary-matching criterion will drive the boundaries obtained in different phases to match, special attentions must be paid to the segmentation consistency over the phases. Otherwise, the inconsistency may result in inaccuracy and artifacts along the boundaries.

Our boundary matching scheme imposes a heavy penalty for mismatching but it does not guarantee a perfect match along the boundaries. In order to examine the magnitude of mismatching, we warped the moving and less-moving subregion segmentation masks using the two deformation vector fields produced by the registrations. The warped masks of both subregions were then compared to produce a mismatched voxel mask, which highlights the overlapped voxels as well as the voxels in the gap if any. The total number of mismatched voxels was tallied and compared to the total number of voxels along the boundary. The mismatched

TABLE II. Average over mean distance for all patients between corresponding points in EIH and EEH phases.

(mm)	No reg	BSP no seg	BSP seg	Dem no seg	Dem seg
Mean of all points	3.94	3.52	2.13	2.93	2.07
Mean of lung points only	7.85	3.50	2.78	2.93	2.73
Mean of rib points only	1.98	3.53	1.81	2.92	1.74

TABLE III. Percentage of mismatched boundary voxels after registration with segmentation.

Patients	1	2	3	4
B-spline (%)	0.00	0.52	0.37	0.11
Demons (%)	1.29	1.04	1.11	1.11

boundary voxel percentages for both B-spline and Demons registration with segmentation for all patients are reported in Table III. All the B-spline registrations except one produced less than 0.4% of mismatched voxels, while the Demons runs averaged about 1.1%. The worst case was a Demons registration, which had 1.29% of voxels mismatched along the boundary. An erosion operation on the mismatched voxel mask with a structure element of radius of one voxel resulted in no highlighted voxel left for all the cases. It indicates that the mismatch along the boundary was at most within two voxels wide. We felt such a degree of mismatch along the boundaries is acceptable in our applications.

An interesting observation is that with subregions being registered separately, it is possible to independently tune the registration algorithm for each subregion. We have performed a limited study to test this, but were not able to achieve consistently better results. However, this approach should be better in practice and merits future study.

V. CONCLUSIONS

Deformable registration results with and without the segmentation of moving and less-moving subregions on four lung patient 4DCT data sets were presented. Qualitative evaluation of the deformation vector fields reveals that registering the anatomical subregions separately allows the registration to capture discontinuities of the deformation vector field. While the registrations produce similar overall warping in the images, segmentation of subregions generates a more realistic registration in the vicinity of the plural interface. A validation based on identification of homologous points in the lungs and on the ribs was performed and registration using segmented subregions was found to achieve consistently improved accuracy for both B-spline and Demons algorithms in both moving and less-moving subregions.

ACKNOWLEDGMENTS

This work was supported in part by R01 CA 111590 and a Siemens Research Grant.

[a]Electronic mail: zwmedphy@gmail.com

[1]S. Flampouri *et al.*, "Estimation of the delivered patient dose in lung IMRT treatment based on deformable registration of 4D-CT data and Monte Carlo simulations," Phys. Med. Biol. **51**, 2763–2779 (2006).
[2]M. Foskey *et al.*, "Large deformation three-dimensional image registration in image-guided radiation therapy," Phys. Med. Biol. **50**, 5869–5892 (2005).
[3]K. K. Brock *et al.*, "Feasibility of a novel deformable image registration technique to facilitate classification, targeting, and monitoring of tumor and normal tissue," Int. J. Radiat. Oncol. Biol. Phys. **64**, 1245–1254 (2006).
[4]S. Gao *et al.*, "A deformable image registration method to handle distended rectums in prostate cancer radiotherapy," Med. Phys. **33**, 3304–3312 (2006).
[5]W. Lu *et al.*, "Automatic re-contouring in 4D radiotherapy," Phys. Med. Biol. **51**, 1077–1099 (2006).
[6]J. R. McClelland *et al.*, "A continuous 4D motion model from multiple respiratory cycles for use in lung radiotherapy," Med. Phys. **33**, 3348–3358 (2006).
[7]D. Sarrut, "Deformable registration for image-guided radiation therapy," Z. Med. Phys. **13**, 285–297 (2006).
[8]W. Y. Song *et al.*, "Dosimetric evaluation of daily rigid and nonrigid geometric correction strategies during on-line image-guided radiation therapy (IGRT) of prostate cancer," Med. Phys. **34**, 352–365 (2007).
[9]A. Trofimov *et al.*, "Temporo-spatial IMRT optimization: Concepts, implementation and initial results," Phys. Med. Biol. **50**, 2779–2798 (2005).
[10]E. Rietzel *et al.*, "Four-dimensional image-based treatment planning: Target volume segmentation and dose calculation in the presence of respiratory motion," Int. J. Radiat. Oncol. Biol. Phys. **61**, 1535–1550 (2005).
[11]P. J. Keall *et al.*, "Monte Carlo as a four-dimensional radiotherapy treatment-planning tool to account for respiratory motion," Phys. Med. Biol. **49**, 3639–3648 (2004).
[12]H. Wang *et al.*, "Validation of an accelerated 'demons' algorithm for deformable image registration in radiation therapy," Phys. Med. Biol. **50**, 2887–2905 (2005).
[13]Y. Yang *et al.*, "Evaluation of on-board kV cone beam CT (CBCT)-based dose calculation," Phys. Med. Biol. **52**, 685–705 (2007).
[14]K. K. Brock *et al.*, "Accuracy of finite element model-based multi-organ deformable image registration," Med. Phys. **32**, 1647–1659 (2005).
[15]M. M. Coselmon *et al.*, "Mutual information based CT registration of the lung at exhale and inhale breathing states using thin-plate splines," Med. Phys. **31**, 2942–2948 (2004).
[16]T. Guerrero *et al.*, "Intrathoracic tumour motion estimation from CT imaging using the 3D optical flow method," Phys. Med. Biol. **49**, 4147–4161 (2004).
[17]W. Lu *et al.*, "Fast free-form deformable registration via calculus of variations," Phys. Med. Biol. **49**, 3067–3087 (2004).
[18]C. R. Meyer *et al.*, "Demonstration of accuracy and clinical versatility of mutual information for automatic multimodality image fusion using affine and thin-plate spline warped geometric deformations," Med. Image Anal. **1**, 195–206 (1997).
[19]V. Pekar, E. Gladilin, and K. Rohr, "An adaptive irregular grid approach for 3D deformable image registration," Phys. Med. Biol. **51**, 361–377 (2006).
[20]E. Rietzel and G. T. Y. Chen, "Deformable registration of 4D computed tomography data," Med. Phys. **33**, 4423–4430 (2006).
[21]D. Rueckert *et al.*, "Nonrigid registration using free-form deformations: Application to breast MR images," IEEE Trans. Med. Imaging **18**, 712–721 (1999).
[22]J. P. Thirion, "Image matching as a diffusion process: An analogy with Maxwell's demons," Med. Image Anal. **2**, 243–260 (1998).
[23]J. B. A. Maintz and M. A. Viergever, "A survey of medical image registration," Med. Image Anal. **2**, 1–36 (1998).
[24]D. L. G. Hill *et al.*, "Medical image registration," Phys. Med. Biol. **46**, R1–R45 (2001).
[25]R. H. Byrd, P. Lu, and J. Nocedal, "A limited memory algorithm for bound constrained optimization," SIAM (Soc. Ind. Appl. Math.) J. Sci. Stat. Comput. **16**, 1190–1208 (1995).
[26]B. Li *et al.*, "Establishing a normative atlas of the human lung: Intersubject warping and registration of volumetric CT images," Acad. Radiol. **10**, 255–265 (2003).
[27]G. K. Matsopoulos *et al.*, "Thoracic non-rigid registration combining self-organizing maps and radial basis functions," Med. Image Anal. **9**, 237–254 (2005).
[28]D. Sarrut *et al.*, "A comparison framework for breathing motion estimation methods from 4D imaging," IEEE Trans. Med. Imaging **26**(12), 1636–1648 (2007).
[29]J. A. Little, D. L. G. Hill, and D. J. Hawkes, "Deformations incorporating rigid structures," Comput. Vis. Image Underst. **66**, 223–232 (1997).

[30]V. Arsigny, X. Pennec, and N. Ayache, "Polyrigid and polyaffine transformations: A novel geometrical tool to deal with non-rigid deformations—Application to the registration of histological slices," Med. Image Anal. **9**, 507–523 (2005).

[31]O. Commowick *et al.*, "An efficient locally affine framework for the registration of anatomical structures," Third IEEE International Symposium on Biomedical Imaging (ISBI 2006), Arlington, VA, 2006 (unpublished).